A Computational Fluid Dynamics and Experimental Investigation of a CT9 Turbocharger Compressor at Low Rotational Speeds

Pham Hoang Anh
Vinh Long University of Technology Education, Vinh Long, Vietnam
anhph@vlute.edu.vn

Le Hong Ky
Vinh Long University of Technology Education, Vinh Long, Vietnam
kylh@vlute.edu.vn (corresponding author)

Received: 21 January 2026 | Revised: 14 February 2026, 1 March 2026, and 5 March 2026 | Accepted: 6 March 2026

Licensed under a CC-BY 4.0 license | Copyright (c) by the authors | *DOI: https://doi.org/10.48084/etasr.17681*

ABSTRACT

This study provides the first validated Computational Fluid Dynamics (CFD)-experimental dataset for the CT9 compressor in the low-speed range of 10,000-20,000 rpm. Steady-state compressible Reynolds-Averaged Navier–Stokes (RANS) simulations were performed using the SST k–ω turbulence model following a verified mesh independence study. Pressure ratio and temperature rise measurements were obtained using a controlled gas stand test facility. The numerical results show strong agreement with the experimental pressure ratio data, the deviations in the isentropic efficiency are primarily due to mechanical losses and thermal effects. The results establish a reliable performance benchmark and improve the understanding of compressor behavior under turbo-lag-related operating conditions.

Keywords-turbocharger compressor; CT9, CFD; isentropic efficiency; low-speed operation

I. INTRODUCTION

The increase of incoming air density in automotive turbocharging systems directly influences the engine's power output, fuel efficiency, and transient response. The performance of the compressor at low rotational speeds is particularly critical, as it affects turbo-lag behavior and drivability under real-world operating conditions. Therefore, accurate prediction of pressure ratio, temperature rise, and isentropic efficiency is essential for reliable performance evaluation. Authors in [1-6] used Computational Fluid Dynamics (CFD) to analyze the internal flow structures and thermodynamic characteristics of centrifugal compressors. Three-dimensional Reynolds-Averaged Navier–Stokes (RANS)-based simulations enable the detailed prediction of pressure distribution, velocity fields, and efficiency characteristics. The SST k–ω turbulence model has demonstrated strong capability in turbomachinery applications involving adverse pressure gradients and separated flows [7]. However, CFD predictions are still sensitive to the turbulence modeling strategy, mesh resolution, and boundary condition assumptions used, which makes experimental validation indispensable. Authors in [8, 9] used gas stand facilities, providing direct measurements of pressure, temperature, and mass flow rate for assessing compressor performance. Authors in [10] showed that heat transfer effects and measurement uncertainties can significantly impact efficiency evaluations, especially at low pressure ratios. Standardized procedures, such as SAE J1826 and ISO 5389, further emphasize the need for rigorous experimental validation of turbo compressor performance [11-14]. Despite extensive research on nominal and high rotational speeds, there is a lack of validated combined CFD-experimental data in the low-speed range below 20,000 rpm, particularly for compact automotive turbochargers such as the CT9 model. This study presents a validated CFD–experimental dataset for a CT9 turbocharger compressor operating between 10,000 rpm and 20,000 rpm. By systematically combining mesh-converged numerical simulations with controlled experimental measurements, the present study establishes a reliable low-speed performance benchmark and advances the understanding of compressor behavior in turbo-lag-dominated conditions.

II. METHODOLOGY

A. Compressor Isentropic Efficiency

In automotive turbochargers, the compressor operates at high speeds. Aerodynamic losses, flow separation, and internal friction cause irreversible effects and generate additional heat.

Consequently, the actual outlet temperature of the compressed air exceeds that of an ideal isentropic compression process [12-14]. Compressor performance is typically evaluated using isentropic efficiency, which is defined as the ratio of the ideal isentropic enthalpy rise to the actual enthalpy rise:

$$\eta_{is} = \frac{T_{3s} - T_1}{T_3 - T_1} \quad (1)$$

Assuming that air behaves as an ideal gas with constant specific heats, the outlet temperature for the isentropic compression process can be expressed as:

$$T_{3s} = T_1 \left(\frac{P_3}{P_1}\right)^{\frac{\gamma-1}{\gamma}} \quad (2)$$

where P_1 and P_3 are the absolute inlet and outlet pressures of the compressor, respectively, and γ is the specific heat ratio of air ($\gamma \approx 1.4$). The compressor outlet temperature (T_3) is measured immediately downstream of the compressor and upstream of the intercooler. While the intercooler significantly affects intake air density and engine performance, it does not impact compressor efficiency.

B. Governing Equations

The flow is assumed to be turbulent and governed by the RANS equations for an ideal gas. Reynolds decomposition is applied to all instantaneous flow variables, resulting in the appearance of the Reynolds stress tensor. This tensor is modeled using the SST k–ω turbulence model [15]. The SST k–ω turbulence model was used for all simulations. This formulation improves the prediction of adverse pressure gradients and flow separation, which are common in centrifugal compressor flows, especially at low rotational speeds. The model ensures robust near-wall resolution and enhanced accuracy in rotating turbomachinery applications. Therefore, it was selected as the turbulence closure model for this study [16]. Heat transfer is modeled by solving the energy equation and accounting for convective and conductive heat transfer within the fluid domain [17]. Rotational effects were incorporated using the Moving Reference Frame (MRF) approach. This method introduces Coriolis and centrifugal force terms into the governing equations, enabling the simulation of steady-state rotating components without mesh motion [18].

III. SIMULATION AND EXPERIMENTAL SETUP

A. Numerical Simulation

1) Problem Modeling

The simulation was performed using STAR-CCM+ software. First, a 3D model was used to accurately depict the airflow within the compressor, as shown in Figure 1 (a). The simulations used a steady-state, compressible, RANS formulation. Air was modeled as an ideal compressible gas, and the SST k–ω turbulence model was employed due to its ability to effectively predict adverse pressure gradients and separated flows, which are commonly encountered in centrifugal compressors. Polyhedral meshers were used to represent the vortex and rotation of the flow. Thin meshers, an efficient form of thin solid mesh, were employed to significantly reduce the number of mesh cells and thus reduce computation time, as depicted in Figures 1 (b) and 2.

2) Boundary Conditions

- Inlet: Total pressure and total temperature
- Outlet: Static pressure
- Rotational speeds: 10,000, 15,000, and 20,000 rpm

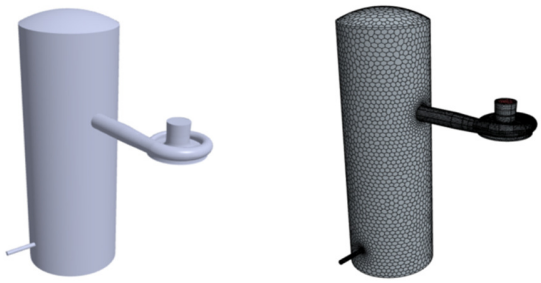

(a) (b)

Fig. 1. (a) Compressor geometry and (b) computational mesh.

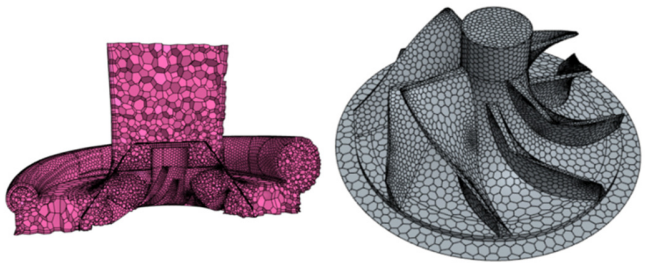

(a) (b)

Fig. 2. Mesh compressor wheel. Vector plots reveal 30% less recirculation (reverse flow) areas: (a) volume through the center of the compressor, (b) compressor wheel.

3) Turbulent Flow and Energy Model

Air was modeled as a compressible ideal gas. The density was calculated according to the ideal gas law ($\rho = p/RT$), where p is the static pressure, T is the temperature, and R is the universal gas constant. This formulation accounts for density variations due to changes in pressure and temperature within the compressor flow field. This is necessary for accurately predicting thermodynamic performance parameters, such as pressure ratio and efficiency.

- Turbulent model: The SST k–ω model was chosen because it easily converges, accurately simulates vortex flow, and is suitable for compressor problems.
- Turbulent viscosity ratio: The initial value was set to 10, representing the ratio of turbulent to kinematic viscosity of the gas.
- Energy model: This model was used to calculate temperature changes during gas compression to accurately simulate compression efficiency and heat loss.

4) Solver

A steady-state solver with an MRF approach is used to model the uniformly rotating compressor wheel without mesh motion. The solution method is segregated flow, which breaks the problem down into separate steps for velocity, pressure, and energy. The energy equation is coupled to accurately simulate the interaction between flow and temperature. During simulation, the system is considered convergent when:

- Calculation errors (residuals) are less than 10^{-4}.
- The output pressure and temperature no longer vary over time.

5) Grid Independence and Mesh Quality

A grid independence study was conducted to evaluate the influence of mesh resolution on predicted compressor performance. Three mesh densities, consisting of 1,287,358 (coarse), 2,120,788 (medium), and 3,461,935 (fine) cells, were analyzed at 20,000 rpm, as illustrated in Table I. The predicted pressure ratios were 1.0084, 1.0093, and 1.0095 for the coarse, medium, and fine meshes, respectively. The corresponding isentropic efficiencies were 35.65%, 35.91%, and 35.92%, respectively. The relative difference between the medium and fine meshes was approximately 0.02% for the pressure ratio and 0.03% for the efficiency. This indicates that the results are not sensitive to further mesh refinement. Thus, the medium mesh was chosen for all subsequent simulations to achieve an optimal balance of computational cost and numerical accuracy. Convergence was achieved with residuals reduced below 10^{-5} and stabilized performance parameters prior to data extraction.

TABLE I. MESH INDEPENDENCE ANALYSIS RESULTS

Mesh	Cells	Pressure Ratio	Isentropic Efficiency (%)
Coarse	1,287,358	1.0084	35.65
Medium	2,120,788	1.0093	35.91
Fine	3,461,935	1.0095	35.92

B. Experimental Setup

This experiment used the compressor from the CT9 turbocharger of the Toyota 3C engine. The compressor wheel was designed and manufactured based on the established basic parameters of the surface model, as portrayed in Figure 3.

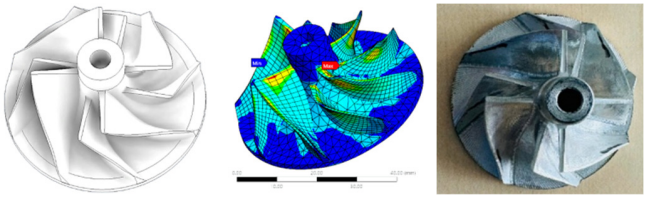

(a) (b) (c)

Fig. 3. Manufactured compressor wheel used in the experiments: (a) design drawing, (b) strength testing, and (c) machine detail.

This study uses an electric motor and an accumulator as the power source for the load to investigate the compressor performance of the turbocharger at low speeds. Inlet and outlet sensors collect pressure and temperature signals. A computer with software is used to process the collected signals, as shown in Figure 4. The pressure sensors utilized in the test bench have an accuracy of ±0.25% full scale, and the thermocouples have an uncertainty of ±1°C. Considering sensor accuracy and data acquisition resolution, the combined uncertainty in pressure ratio was estimated to be within ±0.5%. The propagated uncertainty in isentropic efficiency is approximately ±2%, primarily due to sensitivity to temperature and pressure variations at low pressure ratios. These uncertainty levels are acceptable for evaluating the performance of low-speed compressors and do not affect the overall trend when compared with CFD results.

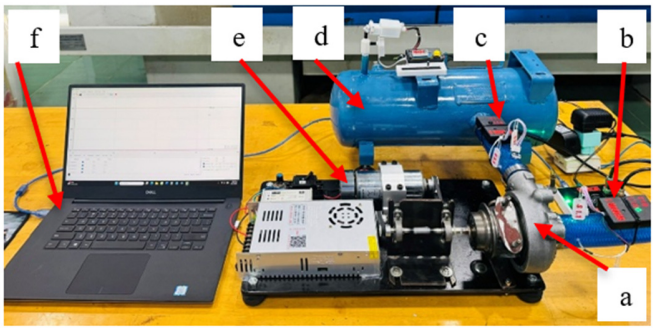

Fig. 4. Experimental setup of the CT9 compressor test bench: (a) compressor, (b) inlet sensor, (c) outlet sensor, (d) accumulator, (e) electric motor, and (f) computer.

IV. RESULTS AND DISCUSSION

A. Simulation Results

The analysis of the simulation results was conducted at three speeds: 10,000 rpm, 15,000rpm, and 20,000 rpm, according to the following main parameters: pressure, temperature, mass flow rate, and flow field (turbulence and velocity).

1) Pressure

Figure 5 displays the inlet pressure (P_1, blue line), outlet pressure (P_2, yellow line), and outlet pressure (P_3, red-blue line) of the compressor at different rotational speeds of the central shaft.

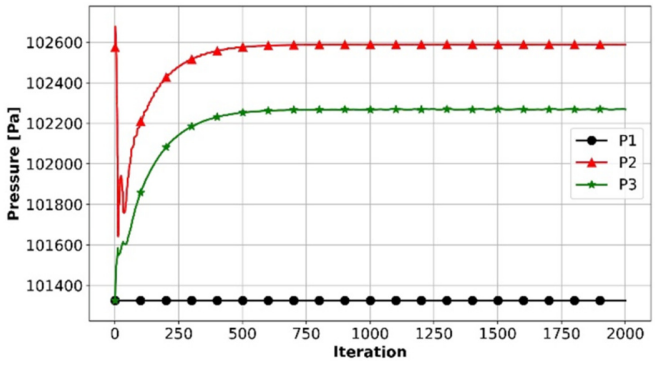

Fig. 5. Comparison of pressure ratio between CFD and experiment.

The results indicate that within the investigated speed range, the pressure at the inlet (P_1) remains stable. Meanwhile, the pressures at the outlet (P_2 and P_3) initially change and then stabilize at a level higher than P_1. Specifically, P_2 is always greater than P_3. The accumulator acts as a "buffer" for the gas flow, stabilizing the pressure by reducing fluctuations and increasing the average value. The outlet pressure increased from 101,325 Pa to 102,269 Pa at 20,000 rpm. These results suggest that the accumulator contributes to pressure stabilization, maintaining a high and consistent pressure suitable for practical applications such as automotive engines.

2) Temperature

The output temperature increases with rotational speed due to the heat generated during gas compression (according to the ideal gas law, stronger compression results in higher temperature). Thanks to the accumulator absorbing and dissipating thermal energy, the temperature is more stable, fluctuating around 301 K with little variation (a slight decrease followed by a return increase). At 20,000 rpm, the temperature difference between the two cases is 3.2 K, as presented in Figure 6.

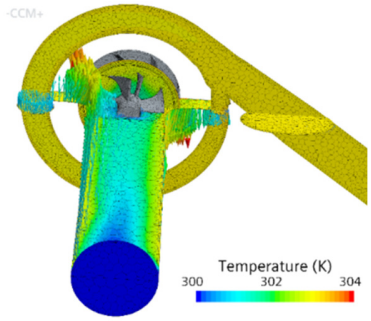

Fig. 6. Outlet temperature variation with rotational speed.

3) Turbulent Flow Field and Velocity

The flow field shows the formation of strong vortices behind the compressor wheel. This is a common phenomenon in centrifugal compressors characterized by concentrated maximum velocity. Vector plots reveal 30% fewer recirculation areas, which significantly improves system stability, as depicted in Figure 7.

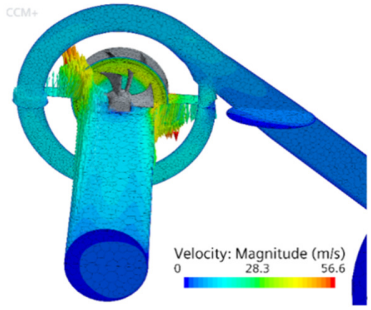

Fig. 7. Velocity magnitude distribution inside the compressor.

4) Isentropic Efficiency

Using the pressure and temperature data obtained at the inlet and outlet corresponding to the three central shaft speeds of the compressor, along with (1) and (2), a summary of compressor efficiency is provided in Table II. The compressor's efficiency increases progressively with rotational speed, indicating its greater ability to compress air as the central shaft spins faster. Efficiency reaches its highest value at 20,000 rpm.

B. Experimental Results

1) Pressure

Figure 8 demonstrates the relationship between input pressure (P_1) and output pressure (P_3) at a speed of 10,000 rpm. Figure 9 portrays the simulated pressure relationship at a speed of 15,000 rpm.

TABLE II. COMPRESSOR EFFICIENCY SUMMARY

n (rpm)	P_1 (Pa)	P_3 (Pa)	T_1 (K)	T_3 (K)	T_{3s} (K)	η_{is} (%)
10000	101325	101625	300	300.8	300.17	21.25%
15000	101325	102027	300	301.8	300.43	23.89%
20000	101325	102589	300	302.2	300.79	35.91%

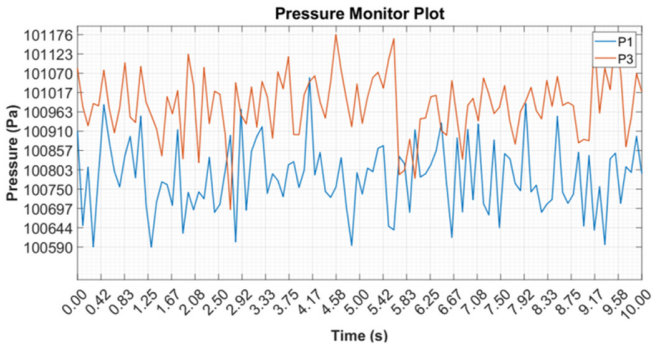

Fig. 8. Inlet/outlet pressure graph at 10000 rpm.

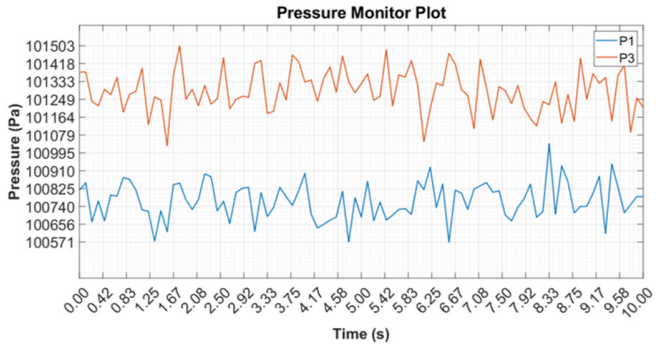

Fig. 9. Inlet/outlet pressure graph at 15000 rpm.

Figure 10 shows that pressure P_1 is always less than pressure P_3. This means that as the speed of the compressor shaft increases, output pressure P_3 increases, while pressure P_1 changes insignificantly. At 20,000 rpm, the difference in output and inlet air pressure P3 becomes apparent. Figure 11 demonstrates that pressure P_1 remains almost constant while pressure P_3 increases rapidly. Considering the low-speed range of the compressor's central shaft, Table II and Figure 12 display the increase in output pressure P_3 with speed.

2) Temperature

Regarding temperature, the experimental results also show an increase in output temperature (T_3) with speed at the low-speed range of the compressor shaft, as illustrated in Table II and Figures 12 and 13. The difference is that the input temperature (T_1) increases with speed as well.

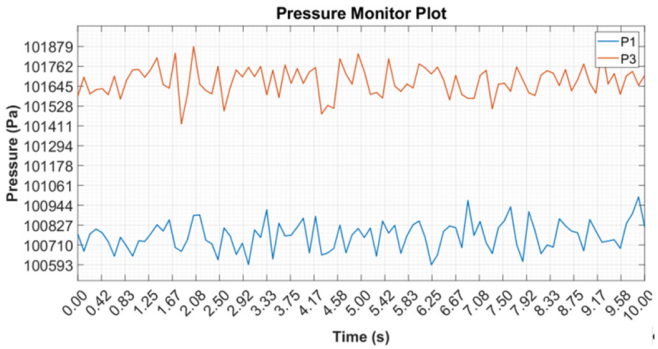

Fig. 10. Inlet/outlet pressure graph at 20000 rpm.

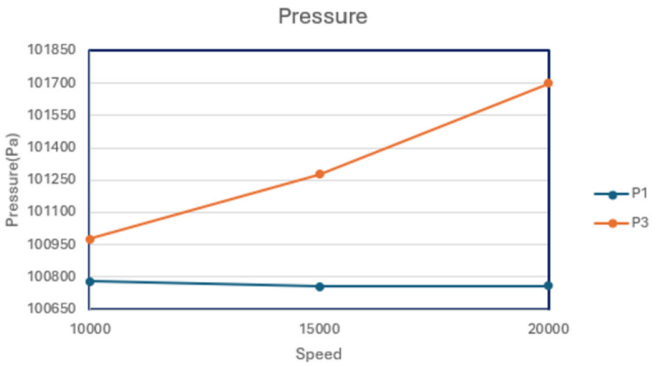

Fig. 11. Relationship between inlet and outlet temperatures and compressor shaft speed.

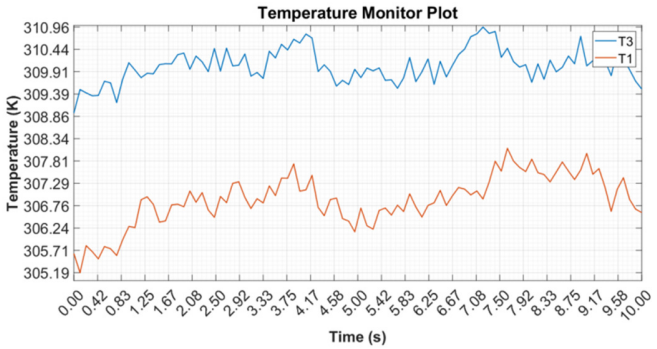

Fig. 12. Temperature at 20000 rpm.

3) Efficiency

Using the pressure and temperature data obtained at the inlet and outlet corresponding to the three central shaft speeds of the compressor, along with (1) and (2), a summary of compressor efficiency is provided in Table III. The compressor's efficiency increases progressively with rotational speed, reflecting its stronger ability to compress air as the central shaft rotates faster. At 20,000 rpm, the efficiency is at its maximum value of 29.05%, whereas at 10,000 rpm, the value is too low, at 9.68%.

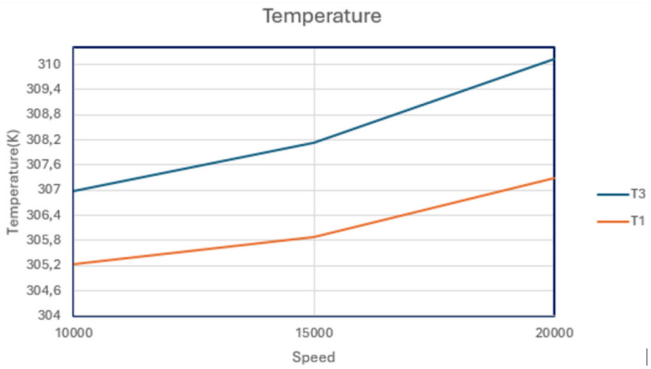

Fig. 13. Relationship between inlet and outlet temperatures and compressor shaft speed.

TABLE III. COMPRESSOR EFFICIENCY SUMMARY

n (rpm)	P_1 (Pa)	P_2 (Pa)	T_1 (K)	T_3 (K)	T_{3s} (K)	η_{is} (%)
10000	100778.8	100974.7	305.225	306.971	305.394	9.68%
15000	100756.5	101276.7	305.895	308.124	306.345	20.19%
20000	100758.5	101699.5	307.303	310.119	308.121	29.05%

C. Summary of Pressure Ratio and Efficiency

Table IV presents the summary of the pressure ratio (P_R) and efficiency (η_i) in both the simulation and experimental cases. The performance discrepancy between the two decreases as speed increases (from 11.57% at 10,000 rpm to 6.86% at 20,000 rpm). This narrowing of the discrepancy confirms that, as speed increases, the actual operating range and the predictive model become more accurate. Figure 14 illustrates the performance characteristics of the CT9 compressor at low speeds as a compression map.

TABLE IV. SUMMARY OF PRESSURE RATIO AND EFFICIENCY

Case	n (rpm)	P_R	η_{is} (%)
Experimental	10000	1.0019	9.68
	15000	1.0051	20.19
	20000	1.0093	29.05
Simulation	10000	1.0023	21.25
	15000	1.0057	23.89
	20000	1.0093	35.91

The relatively low isentropic efficiency observed in the 10,000–20,000 rpm range is due to several physical factors. At low rotational speeds, the compressor operates with reduced blade tip velocity, resulting in weaker energy transfer from the impeller to the working fluid. Additionally, mechanical losses in bearings and shaft systems become more significant relative to the aerodynamic power output. Heat transfer between the compressed air and the compressor casing may also influence efficiency estimation, particularly in low-pressure-ratio conditions, where small temperature variations can significantly affect calculated thermodynamic parameters. Furthermore, evaluating efficiency at very low-pressure ratios

is sensitive to uncertainties in pressure and temperature measurements, which may partially explain the discrepancy between CFD predictions and experimental results. Despite these factors, the consistent performance trend confirms the numerical model's validity for analyzing low-speed operation.

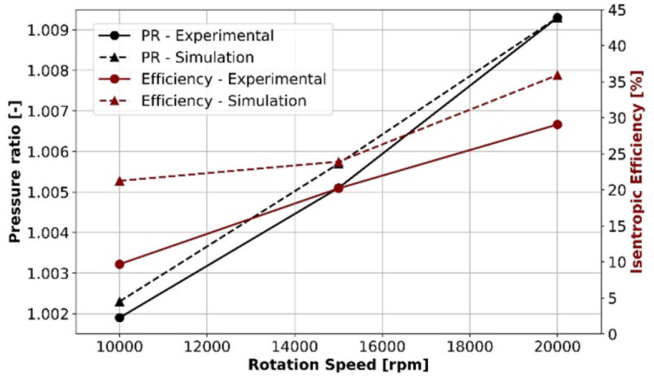

Fig. 14. Performance characteristics of the CT9 compressor at low Speed range.

V. CONCLUSIONS

This study presents a combined Computational Fluid Dynamics (CFD) and experimental investigation of the CT9 turbocharger compressor operating within the low rotational speed range of 10,000–20,000 rpm. Steady-state compressible Reynolds-Averaged Navier–Stokes (RANS) simulations using the SST k–ω turbulence model were validated against 100 experimental data points. The results showed very good agreement in pressure ratio predictions, with deviations below 1%. The efficiency discrepancies were slightly larger and were attributed to mechanical losses, heat transfer effects, and the increased sensitivity of efficiency calculations at near-unity pressure ratios. A grid-independence study confirmed that numerical dissipation is negligible, and an uncertainty analysis quantified the reliability of the experimental measurements. The validated dataset provides new insights into low-speed compressor behavior, which is often underreported in the literature. These findings contribute a physically validated reference dataset for CT9 compressor performance in the low-speed regime, providing a reliable basis for future transient engine and turbo-lag studies.

REFERENCES

[1] M. I. Soliman, A. A. Emara, E. M. Abdel Razek, and H. A. Moneib, "Modeling and CFD Analysis of Air Flow through Automotive Turbocharger Compressor: Analytical Approach and Validation," *Aerospace Sciences & Aviation Technology (ASAT)*, vol. 17, pp. 1–15, Apr. 2017, https://doi.org/10.21608/asat.2017.22756.

[2] B. A. Chandrashekar and A. Bhaduria, "Computational Fluid Dynamics (CFD) Analysis of Turbocharger Aerodynamics and Thermal Behaviour in Automotive Applications," SAE International, Technical, Nov. 2025. https://doi.org/10.4271/2025-28-0229.

[3] X. L. Liu et al., "CFD analysis of internal flow field in turbocharger compressor," *Applied Mechanics and Materials*, vol. 628, pp. 279–282, 2014, https://doi.org/10.4028/www.scientific.net/AMM.628.279.

[4] X. L. Liu, M. X. Liu, and J. K. Gong, "The CFD Analysis of Gasoline Engine Turbocharger Compressor Based on NUMECA," *Applied Mechanics and Materials*, vol. 433–435, pp. 2169–2173, 2013, https://doi.org/10.4028/www.scientific.net/AMM.433-435.2169.

[5] S. Patil and L. B. Rao, "CFD analysis of turbocharger compressor to study the effect of geometry change on surge and performance," *International Journal of Performability Engineering*, vol. 14, no. 1, pp. 9–16, 2018.

[6] M. X. Liu, "CFD analysis of JQ40A gasoline turbocharger compressor," *Applied Mechanics and Materials*, vol. 364, pp. 144–148, 2013, https://doi.org/10.4028/www.scientific.net/AMM.364.144.

[7] M. U. Sohail, M. Hassan, S. H. R. Hamdani, and K. Pervez, "Effects of Ambient Temperature on the Performance of Turbofan Transonic Compressor by CFD Analysis and Artificial Neural Networks," *Engineering, Technology & Applied Science Research*, vol. 9, no. 5, pp. 4640–4648, Oct. 2019, https://doi.org/10.48084/etasr.2998.

[8] S. Kazemi Bakhshmand, L. T. Luu, and C. Biet, "Experimental Energy and Exergy Analysis of an Automotive Turbocharger Using a Novel Power-Based Approach," *Energies*, vol. 14, no. 20, Jan. 2021, Art. no. 6572, https://doi.org/10.3390/en14206572.

[9] G. Tanda et al., "Experimental investigation of turbocharger compressor performance considering heat transfer effects," *Applied Energy*, vol. 164, pp. 806–815, 2016, https://doi.org/10.1016/j.apenergy.2015.12.022.

[10] R. Huang, J. Ni, Q. Wang, X. Shi, and Q. Yin, "Experimental and mechanism study of aerodynamic noise emission characteristics from a turbocharger compressor," *Sustainability*, vol. 15, no. 14, 2023, Art. no. 11300, https://doi.org/10.3390/su151411300.

[11] R. Bontempo et al., "Steady and unsteady experimental analysis of a turbocharger for automotive applications," *Energy Conversion and Management*, vol. 99, pp. 72–80, 2015, https://doi.org/10.1016/j.enconman.2015.04.019.

[12] A. H. Dixon and C. A. Hall, *Fluid Mechanics and Thermodynamics of Turbomachinery*, 7th ed. Oxford, United Kingdom: Elsevier, 2014.

[13] *J1826_202204 - Turbocharger Gas Stand Test Code*. Warrendale, PA, USA: SAE International, 2022.

[14] *5389:2005 Turbocompressors — Performance test code*. Geneva, Switzerland: ISO, 2005.

[15] S. B. Pope, *Turbulent Flows*. Cambridge, United Kingdom: Cambridge University Press, 2000.

[16] F. R. Menter, "Two-equation eddy-viscosity turbulence models for engineering applications," *AIAA Journal*, vol. 32, no. 8, pp. 1598–1605, 1994, https://doi.org/10.2514/3.12149.

[17] T. L. Bergman, *Fundamentals of Heat and Mass Transfer*, 7th ed. Hoboken, NJ, USA: John Wiley & Sons, 2011.

[18] J. H. Ferziger and M. Peric, *Computational Methods for Fluid Dynamics*, 4th ed. Cham, Switzerland: Springer Science & Business Media, 2020.